The EEFIT Remote Sensing Reconnaissance Mission for the February 2023 Turkey Earthquakes

Voelker, Brandon; Milillo, Pietro; Tavakkoliestahbanati, Amin; Macchiarulo, Valentina; Giardina, Giorgia; Recla, Michael; Schmitt, Michael; Cescon, Marzia; Aktas, Yasemin D.; So, Emily

Citation (APA)
Voelker, B., Milillo, P., Tavakkoliestahbanati, A., Macchiarulo, V., Giardina, G., Recla, M., Schmitt, M., Cescon, M., Aktas, Y. D., & So, E. (2024). The EEFIT Remote Sensing Reconnaissance Mission for the February 2023 Turkey Earthquakes. *IEEE Journal of Selected Topics in Applied Earth Observations and Remote Sensing*, *17*, 19160 - 19173. https://doi.org/10.1109/JSTARS.2024.3476029

Important note
To cite this publication, please use the final published version (if applicable).
Please check the document version above.

The EEFIT Remote Sensing Reconnaissance Mission for the February 2023 Turkey Earthquakes

Brandon Voelker , Pietro Milillo , *Senior Member, IEEE*, Amin Tavakkoliestahbanati,
Valentina Macchiarulo , *Member, IEEE*, Giorgia Giardina , Michael Recla , Michael Schmitt ,
Marzia Cescon *, Member, IEEE*, Yasemin D. Aktas, and Emily So

Abstract—Accurate and rapid postearthquake structural damage assessment is of vital importance for humanitarian relief. Remote sensing techniques have the potential to map large areas with reduced data latency but are limited by several factors, including accuracy (compared to in-situ monitoring campaigns) and data acquisition frequency. Current damage assessment techniques relying on remote sensing data enable rapid assessment in situations where on-site reconnaissance is not possible or desirable. Yet, these techniques rely on different scales, measurement methods, and spatial resolutions, making it difficult to assimilate many different damage products in a homogeneous damage map. Here, we present the results of the U.K.'s Earthquake Engineering Field Investigation Team's remote-sensing-based reconnaissance mission, which was carried out in the aftermath of the series of earthquakes that struck Turkey and Syria in February 2023. We use a set of publicly available damage maps based on synthetic aperture radar, optical imaging, and ground-based reports as well as in-house developed damage products and assess their relative accuracies. We describe the process of supporting on-site reconnaissance planning by creating maps that describe the building stock and diversity of damage in southeast Turkey to assist field survey teams in selecting regions that represent a diverse sample of building typologies and damage levels. Our results show that satellite-based remote sensing damage maps disagree with each other, and extensive validation data are still required to characterize the accuracy of each method at both high and medium resolution. Finally, we provide recommendations for planning and validation of future earthquake response efforts.

Index Terms—Damage assessment, earthquake, remote sensing, Turkey.

I. Introduction

ON 6 February 2023, two powerful earthquakes of Mw 7.8 and 7.5 struck a wide region in southeastern Türkiye and northern Syria, killing over 55 000 people with a very destructive impact on the built environment. The postdisaster engineering community responded promptly, including the U.K.'s Earthquake Engineering Field Investigation Team (EEFIT), which assembled a team comprising individuals from academic and industrial backgrounds from across the globe [1], [2]. The team organized itself into several working groups, including remote sensing, which was characterized by two main goals: 1) assisting the ground-based teams in selecting the most relevant areas of interest (AOIs) to conduct field surveys and 2) developing a replicable framework to identify, apply, and validate suitable remote sensing approaches, methodologies, and datasets to assist postearthquake reconnaissance missions [2]. We adopted a hybrid approach where selected team members provide support remotely, while a smaller group travels to the affected area [3].

Hybrid missions gained their popularity during the COVID-19 pandemic as a response to the disruption in international travel, which posed challenges to the disaster risk resilience community [3], [4], [5]. Along with other alternative data sources, such as digital photography, GPS positioning, the internet, mobile phone networks, high-resolution satellite reconnaissance, social media, and crowdsourcing platforms [6], [7], [8], [9], [10], remote sensing is now a central part of hybrid reconnaissance missions, confirming the viability of the available technology and datasets to effectively support earthquake field missions. While the development of remote sensing methods, especially those based on optical and radar imagery, does not reduce the value of close-range damage mapping from field operators [11], timely and accurate remote sensing data analysis allows teams to organize field operations with the

Brandon Voelker and Amin Tavakkoliestahbanati are with the Department of Civil & Environmental Engineering, University of Houston, Houston, TX 77204 USA (e-mail: bvoelker@uh.edu; atavakk3@cougarnet.uh.edu).

Pietro Milillo is with the Department of Civil & Environmental Engineering, University of Houston, Houston, TX 77204 USA, also with the German Aerospace Center (DLR), Microwaves and Radar Institute, 82234 Munich, Germany, and also with the Centro Euro Mediterraneo Sui Cambiamenti Climatici, 73100 Lecce, Italy (e-mail: pmilillo@central.uh.edu).

Valentina Macchiarulo and Giorgia Giardina are with the Department of Geoscience and Engineering, Delft University of Technology, 2628 Delft, Netherlands (e-mail: v.macchiarulo@tudelft.nl; g.giardina@tudelft.nl).

Michael Recla and Michael Schmitt are with the Institute of Space Technology & Space Applications, Bundeswehr University Munich, 85577 Neubiberg, Germany (e-mail: michael.recla@unibw.de; michael.schmitt@unibw.de).

Marzia Cescon is with the Department of Mechanical Engineering, University of Houston, Houston, TX 77204 USA (e-mail: mcescon2@central.uh.edu).

Yasemin D. Aktas is with the Department of Civil, Environmental & Geomatic Engineering, University College London, WC1E 6BT London, U.K. (e-mail: y.aktas@ucl.ac.uk).

Emily So is with the Department of Architecture, University of Cambridge, CB2 1PX Cambridge, U.K. (e-mail: ekms2@cam.ac.uk).

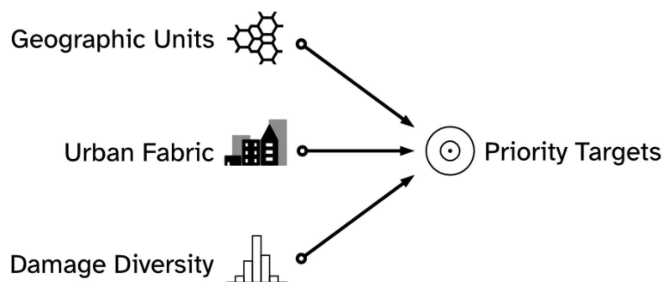Digital Object Identifier 10.1109/JSTARS.2024.3476029

Fig. 1. Strategy employed in the remote mission to provide actionable data to make informed recommendations to ground-based survey teams. Field survey locations were determined using data sources representing three themes: geographic units, urban fabric, and damage diversity.

support of a continuous stream of remote sensing products [12]. As an example, building-by-building damage mapping driven by remote sensing datasets has been an important component of some reconnaissance missions aimed at assessing damage and empirical relationships for loss estimation [11], [13], [14]. State-of-the-art remote sensing technology has begun to contribute to earthquake damage mapping, making early assessments possible and shaping the structure and content of reconnaissance missions in terms of event characterization and damage assessment [6].

In this article, we aim to assess the suitability of remote sensing products in generating damage assessments using currently available satellite constellations for postdisaster evaluation. The rest of this article is organized as follows. In Section II, we describe the data used in this article, while Section III presents the remote-sensing-based approach developed for selecting potential AOIs for the EEFIT group traveling to the regions affected by the 2023 events. Section IV describes the intercomparison between different damage mapping techniques and validations with ground-based EEFIT data. Finally, Section V concludes this article.

II. DATA

The main concern in the immediate aftermath of earthquakes is to assist field teams in selecting AOIs for surveys. To this end, we typically develop a repository of the most up-to-date information from humanitarian reference data, satellite imagery, and damage maps in order to inform this selection. Our approach required collecting three types of data (Fig. 1). First, geographic units (Section II-A) are required mainly to serve as the input for zonal statistics, as well as for data visualization and aggregation. Next, information on the urban fabric (Section II-B) is used to characterize the distribution of building age, size, height, extent, and density within cities. Last, damage proxy maps (DPMs) (Sections II-C–II-E) can be used to assess the variance of damage within each geographic unit. Ground-based validation datasets are described in Section II-F. The datasets listed in Table I represent those that were used during the EEFIT reconnaissance mission to the February 2023 Türkiye earthquakes.

With the available satellite data sources, we generated synthetic aperture radar (SAR) DPMs using the Argentinian L-Band SAOCOM SAR satellite (Section II-D) [15], [16], artificial intelligence (AI) damage maps over individual buildings using very high resolution (VHR) SAR intensity images from Capella Space (Section II-E) [14], and building height maps using a deep-learning-based single-image height reconstruction from VHR SAR Umbra Space data (Section II-G) [17].

A. Geographic Units

The Humanitarian Data Exchange [18] provides subnational administrative boundaries for Türkiye. Level 1 boundaries encompass the largest area, usually representing national provinces, while lower level boundaries represent smaller administrative units. In order to aggregate all the available datasets relating to the urban fabric (Section II-B) and earthquake damage (Sections II-C, II-D, and II-F), we used the smallest boundary level available for southwest Türkiye, Level 3. The average area of the 8657 districts in the study area is 11.2 km^2, with a median of 7.2 km^2 and standard deviation of 18.6 km^2.

B. Urban Fabric

To obtain information on the built-up areas in the southeastern provinces of Türkiye affected by the February 2023 earthquakes, we used the World Settlement Footprint three-diensional 3-D (WSF 3-D) from the German Aerospace Center (DLR), which provides global raster data of urban areas at 90-m resolution, within each pixel [19]. There are four datasets, representing the total area, height, volume, and fraction of buildings within each pixel. As building codes change over time, it is important to understand where structures that predate existing seismic codes are located. To this end, we employed the WSF evolution dataset [20], which depicts the physical extent of settlements every year from 1985 to 2015 at 30-m resolution. We downloaded the WSF 3-D and evolution images as $1° \times 1°$ GeoTiff tiles over southeast Türkiye. We also made use of a database comprising 4.8 million building footprints in Türkiye, created by the Humanitarian OpenStreetMap Team (HOT), and provided by the Humanitarian Data Exchange [21].

C. Optical Damage Maps From CEMS and Microsoft

Rapid response products created from VHR (<1-m resolution) optical satellite images for humanitarian purposes are freely provided by Copernicus Emergency Management Service (CEMS). We downloaded all 37 damage grading products from activation EMSR648 [22], which mapped 20 cities in southeast Türkiye near the earthquake epicenter using imagery sourced from Pléiades WorldView-2 and ESRI World Imagery. The postevent images were acquired for the period of 7–9 February 2023. These maps consist of 49 116 points corresponding either to buildings or to city blocks, labeled according to damage grade. The building damage was manually assessed through photointerpretation of the optical imagery. CEMS modified the EMS-98 scale [23] to account for the limitations of remotely sensed imagery and rapid assessment, resulting in the categories "no visible damage," "possibly damaged," "damaged," and "destroyed" [24], [25].

TABLE I
ALL DATASETS USED FOR THIS ARTICLE

Dataset	Publisher	Format	Description	Source
OpenStreetMap Buildings [21]	Humanitarian Data Exchange	Polygon	Database of 4.8 million building polygons in Türkiye.	Publicly available data
Türkiye Subnational Administrative Boundaries [18]	Humanitarian Data Exchange	Polygon	Administrative boundaries ranging from large (Level 1) to small (Level 3).	Publicly available data
World Settlement Footprint (WSF) 3-D [19], [40]	German Aerospace Center (DLR)	Raster	Globally available average height, volume, area and the fraction of buildings with 90-m pixels.	Publicly available remote sensing data
World Settlement Footprint (WSF) Evolution [20]	German Aerospace Center (DLR)	Raster	Yearly global estimates of human settlement extents from 1985 to 2015.	Publicly available remote sensing data
Official damage maps from Turkish government [33]	Turkish Ministry of Environment, Urbanization and Climate Change (CSB)	Point	Damage maps from nationwide postseismic data collection effort.	Ground-based data
EEFIT Field Mission [2]	EEFIT	Point	EEFIT reconnaissance mission from 13–17 March 2023.	Ground-based data
ARIA DPM [29]	NASA/JPL/Caltech	Raster	Coherence-based DPM using Copernicus Sentinel-1 data.	Publicly available remote sensing data
SAOCOM Coherence DPM	This study	Raster	Coherence-based DPM using co-seismic and post-seismic imagery.	In-house data
Copernicus EMS Activation EMSR648 [22]	Copernicus Emergency Management Service	Point	Rapid response damage maps from very-high resolution (under 1 m) optical data over 20 AOIs near the EQ epicenters.	Publicly available remote sensing data
AI-based building damage assessment [26]	Microsoft	Polygon	High-resolution optical imagery was used to classify damaged buildings with convolutional neural networks.	Publicly available remote sensing data
Integration of very high resolution SAR imagery and machine learning [14]	Macchiarulo et al., [14]	Polygon	Random forest classification of building damage using VHR SAR data.	In-house data
AI-derived building heights [17]	This study	Raster	Post-earthquake building height maps derived from VHR Umbra SAR data.	In-house data

Immediately after the earthquake, a team led by the Microsoft AI for Good Lab applied AI techniques to detect damaged buildings [26]. Using imagery from 7–9 February 2023, sourced from Planet Labs and Maxar Technologies at spatial resolutions of 50 and 30 cm, respectively, a convolutional neural network (CNN) was used to classify the imagery as part of a damaged building, part of an undamaged building, or neither. Then, the percentage of damaged area within each damaged building footprint was calculated.

D. InSAR Damage Proxy Maps

Interferometric synthetic aperture radar (InSAR) coherence measures phase quality between a pair of images, derived from the complex values of corresponding pixels [27], [28]. The coherence between two acquisitions in an urban environment is expected to be high unless there is an abrupt change, such as structural damage. If the provided InSAR pairs are characterized by similar temporal baseline, a coseismic pair of images (one acquired before and one after the earthquake) will have a lower coherence than a preseismic or postseismic pair [15]. Positive values in the DPM depict damaged areas, with higher values indicating more significant damage. Negative values are mostly due to temporal decorrelation, and not earthquake damage, and therefore cannot be interpreted as damaged areas.

We acquired a DPM produced by the Advanced Rapid Imaging and Analysis (ARIA) team at NASA's Jet Propulsion Laboratory and California Institute of Technology in Southern California. The map was produced using 30-m resolution C-band SAR images from Sentinel-1 satellites, operated by the European Space Agency. The postevent images were taken for 10 February 2023, and pre-event images were taken for a time window between 19 September and 29 January 2022 [29].

In addition to the ARIA DPM, we created a 7-m resolution DPM using the Argentinian spaceborne L-band polarimetric SAR satellite mission, SAOCOM. Comisión Nacional de Actividades Espaciales (CONAE) launched SAOCOM-1A and SAOCOM-1B on 07 October 2018 and 30 August 2020, respectively [30]. Three single look complex HH-polarized descending images, covering an area near Islahiye and acquired for 11-07-2022, 20-02-2023, and 28-02-2023, were used to create InSAR coherence-based DPMs according to the procedure and processing parameters described in [15]. The coseismic and postseismic pairs are most comparable when they have the same temporal baseline since all temporal decorrelation effects will be similar. For the SAOCOM acquisitions, this was not the case, as the temporal baselines differ. We discuss the implications of this in Section V.

E. SAR-Intensity-Based Damage Maps

We utilized a machine-learning approach to identify damage at the building level using postevent VHR Capella Space SAR imagery [14]. A random forest (RF) classifier was used to classify buildings as collapsed or standing. Ten GLCM textural features [31], namely contrast, dissimilarity, homogeneity, angular second moment, energy, maximum probability, entropy, mean, variance, and correlation, were extracted from the VHR Capella SAR amplitude data. Using the SAR images and derived textural features, as well as building footprints from the Microsoft Global ML Building Footprints program [32], training was performed in three steps: standard supervised learning for each case study, combined learning across case studies, and generalization testing. Building damage labels used for training were obtained by CEMS and HOT.

F. Ground-Based Damage Maps From the Turkish Ministry of Environment, Urbanization and Climate Change (CSB) and EEFIT

We also used damage maps developed using the official damage data released by the Turkish Ministry of Environment, Urbanization and Climate Change—Çevre, Şehircilik ve İklim Değişikliği Bakanlığı (CSB) in Turkish—from their large-scale damage assessment campaign. These data were processed by Gece Yazılım and visualized by Yer Çizenler [33]. The data released via the CSB web portal, based on the addresses of each damage-assessed building, provide a damage class for around 1.3 million buildings across the 11 provinces that were impacted by the February 2023 earthquakes. The damage classes are as follows: "slightly damaged," "moderately damaged," "heavily damaged," "needs demolition," and "collapsed." The damage data on the CSB website were updated several times over around a month following the earthquakes, with either new data from the ongoing damage assessment exercise, or from changes to the associated damage class to individual buildings (presumably as a result of reassessment upon objections by the residents). While we cannot be certain of the extent of these amendments due to the lack of an aggregated dataset, the damage map produced by the efforts of Gece Yazılım and Yer Çizenler was last updated on 20 February 2023, and is therefore not fully up to date. It

TABLE II
DAMAGE GRADES USED FOR EACH OF THE VALIDATION DATASETS

Dataset	Grade	Description
CEMS	0	No visible damage
	1	Possibly damaged
	2	Damaged
	3	Destroyed
CSB	1	Slightly damaged
	2	Heavily damaged
	3	Needs to be demolished
	4	Collapsed
EEFIT	0	No damage
	1	Negligible to slight damage
	2	Moderate damage
	3	Substantial to heavy damage
	4	Very heavy damage
	5	Destruction

The CEMS data is comprised of human-made labels from VHR optical imagery, while CSB and EEFIT represent ground-based assessments. For the purposes of binary classification, the highest damage grades, indicated in gray, are considered as collapsed, while all other damage grades (white) are considered standing.

should also be noted that the CSB dataset has been observed to have few moderately damaged cases, arguably due to the protocols on which it is based, leading to damage assessment outcomes skewed towards no/little damage and heavy damage categories [2]. Therefore, we exclude the "moderately damaged" class from our analysis (Table II).

The EEFIT team performed a field-based damage assessment on 13–17 March 2023, using the Fulcrum and Device Magic (DM) data collection mobile apps [1]. The survey was designed to encompass a diverse spectrum of building structural systems and damage types [2]. Damage grades were recorded according to the EMS-98 scale from 1–5 [23]. Grade 1 represents damage that is negligible to slight, 2 represents moderate damage, 3 represents substantial to heavy damage, 4 represents very heavy damage, and 5 represents destruction. A "0" grade was added to represent buildings with no damage. In addition to the damage grade, photographs were taken at each building, and data on latitude, longitude, detailed information on the primary structural system and materials, function (e.g., residential, commercial, public, etc.), and damage mechanisms were recorded.

G. SAR2Height Building Height Maps

We also employed the SAR2Height deep-learning architecture to estimate building heights using VHR SAR imagery [17]. The technique uses a CNN, with the SAR image as the input to the encoder and the output of the decoder being a map of heights above ground, which is equal to a normalized digital surface model. Residual blocks with skip connections, as in ResNet [34], are used to build both the encoder and decoder, along with pooling and unpooling operations. We used VHR SAR data
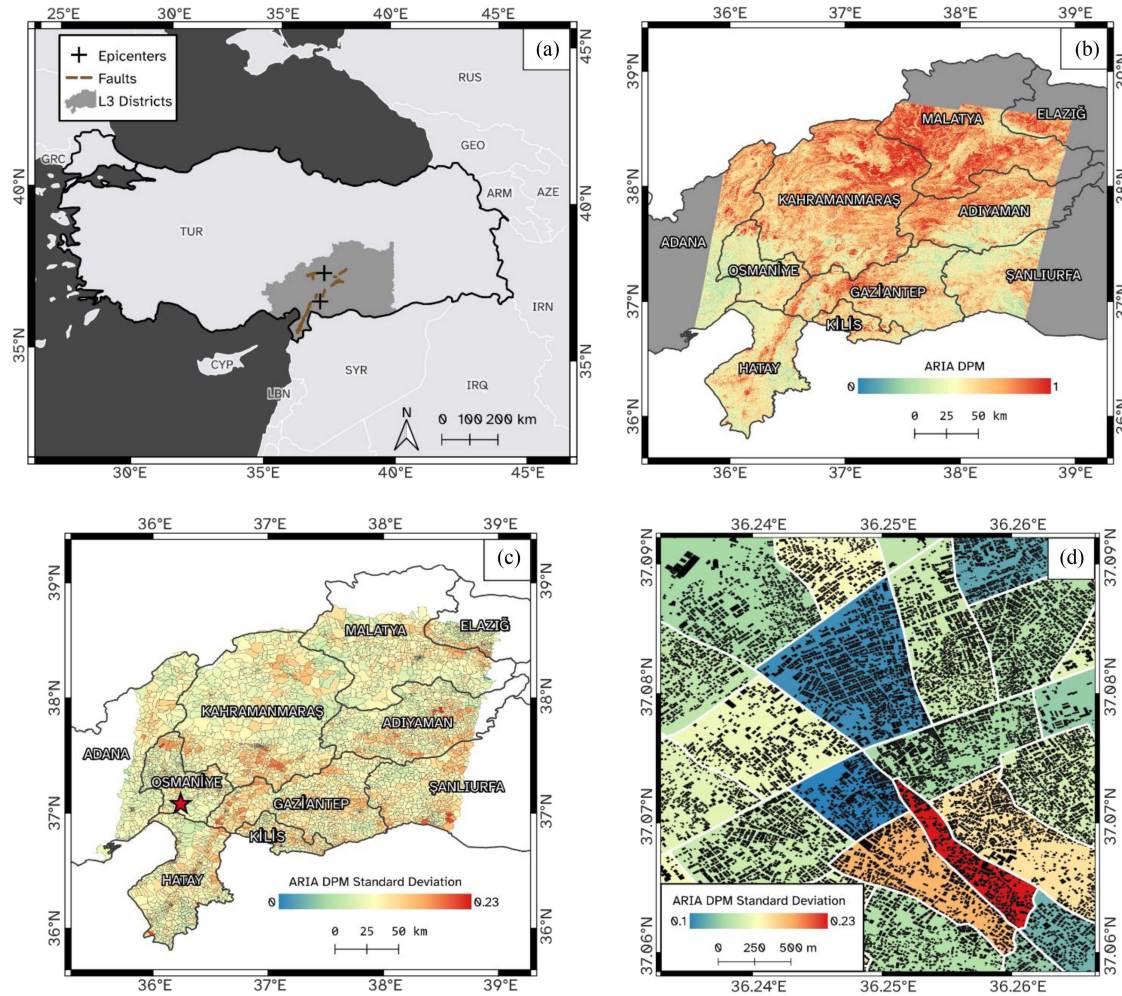
Fig. 2. Visualization of the descriptive mapping pipeline, using the ARIA DPM as an example. Panel (a) shows the study region and extent of the Level 3 (L3) administrative districts. Panel (b) displays the DPM within the AOI in southeast Türkiye, with provinces (Level 1 districts) labeled. Panel (c) shows the standard deviation of the DPM within each L3 district. The red star indicates the location of panel (d), which consists of a zoomed-in view of the DPM standard deviation map within the city of Osmaniye. OpenStreetMap building footprints are shown as black polygons. In panel (c), the L3 district boundaries are light grey, while in panel (d), the same L3 district boundaries are white.

from the Umbra Space commercial microsatellite constellation to create 1-m-resolution building height maps for each major city in the affected region.

III. METHODOLOGY

A. Descriptive Mapping and City Target Selection

Once all the data sources were identified, we extracted descriptive analytics of the affected earthquake region in southeast Türkiye. Using zonal statistics, we described the urban fabric and diversity of damage within the smallest level of administrative boundaries available (Fig. 2). We characterized the nature of the building stock primarily with DLR WSF data, providing insight into the distribution of building age, size, and density [19], [20]. Furthermore, since only a small subset of the total building stock can be surveyed by the field teams in the aftermath of a disaster of this scale, it is important to measure areas characterized by damage diversity where remote sensing techniques might provide dissimilar results. Thus, areas where all buildings were

destroyed, or where all buildings were intact, were avoided, and areas and districts with a certain level of variance in damage were focused on.

We created an automated pipeline to calculate summary statistics for quantitative datasets across southeast Türkiye. Level 3 subnational administrative boundaries (Section II-A) served to define zones, and the values were derived from zonal statistics representing mean or standard deviation of datasets describing the urban fabric (WSF 3-D and WSF Evolution) and damage diversity (ARIA, SAOCOM, Microsoft, CEMS, and CSB damage maps). While Fig. 2 depicts the zonal statistics methodology, which was employed across the entire region for every dataset relating to the urban fabric and building damage (Sections II-B–II-F), Fig. 3 shows a subset of these data over the administrative districts of Islahiye, where the largest number of datasets overlapped. In Fig. 3, Panel A shows the location of the administrative districts, Panels B–D show the mean values of the WSF datasets within each zone, Panel E shows the percentage of buildings that had already been assessed by ground
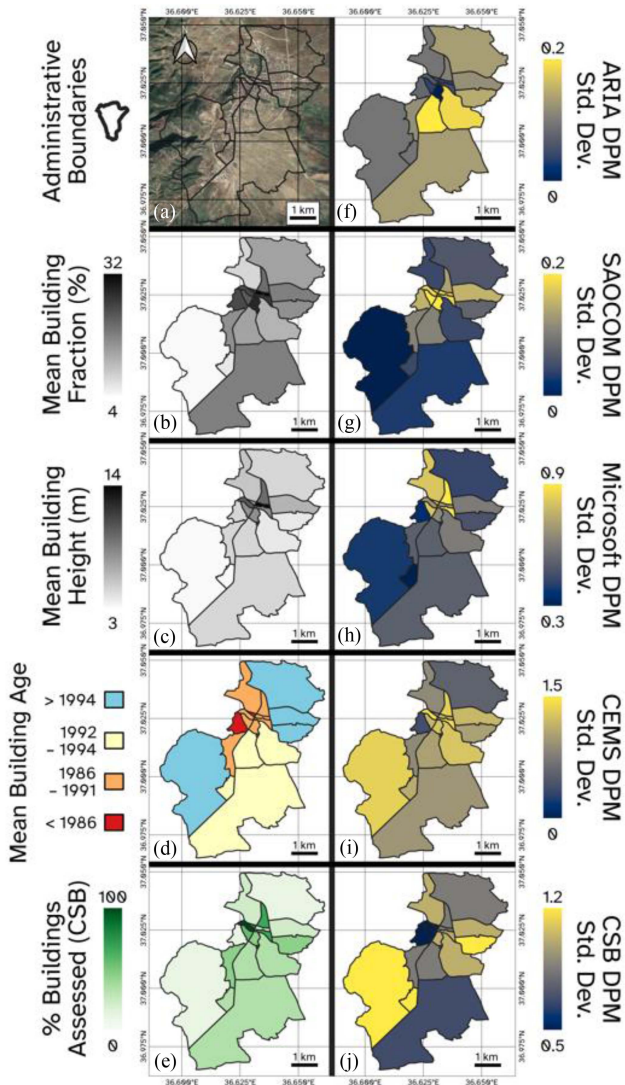
Fig. 3. Descriptive maps for the city of İslahiye, the city where all datasets overlap, displaying different statistics of each dataset within Level 3 administrative boundaries. (a) Google satellite view of the city overlain with administrative boundaries. (b) Mean fraction of buildings per pixel in the DLR WSF 3-D dataset. (c) Mean height of buildings in the DLR WSF 3-D dataset. (d) Average age of buildings per district, with dates classified according to changes in Turkish building codes [2]. (e) Percentage of building stock in each district that was assessed by the CSB data. (f–j) Standard deviation of DPM values or damage grades for ARIA, SAOCOM, Microsoft, CEMS, and CSB.

teams in the CSB data, and Panels F–J describe the standard deviation of each of the damage maps within the districts. At the end of this process, we focused on urban areas characterized by a variety of remotely sensed DPM damage levels and identified the top 11 areas with the largest variance in damage (Fig. 4). The EEFIT team then considered these areas within their visited cities when orchestrating their field trip efforts for gathering ground truths [2].

B. Cross-Comparison of Postdisaster Assessments

To obtain damage values that correspond in geographic location between datasets, we performed pairwise sampling of data
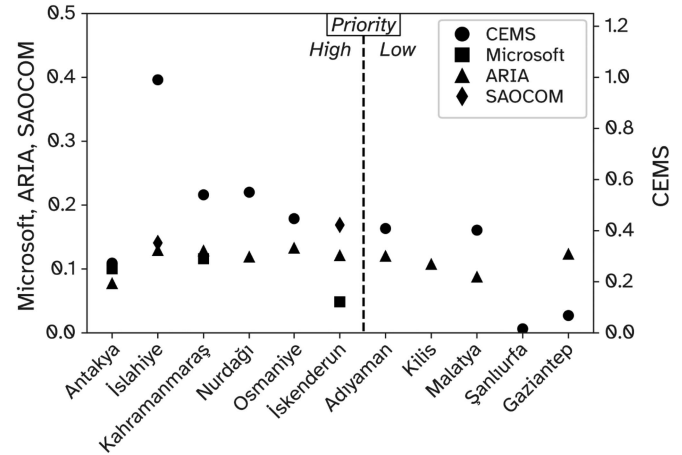

Fig. 4. Normalized DPM standard deviation for each city, averaged across the districts in each city. The microsoft DPM represents the percentage of damaged area within a building footprint [26]. ARIA and SAOCOM derive from coherence-based methods using SAR data [15], [29]. The CEMS damage grade descriptions are available in Table II. Due to logistical considerations, only Antakya, Kahramanmaras, Osmaniye, and Iskenderun were visited.

points between the damage maps described in Sections II-C, II-D, and II-F. The maps varied in format, including vector data (from points to polygons), as well as raster images (Table I). Therefore, several sampling methods were employed: 1) sample points within raster; 2) sample points within polygons; 3) sample point to nearest point; and 4) sample polygon centroid in raster. For instance, in method 1), a point labeled as "collapsed" in the CSB data may have value of 0.8 at the corresponding pixel location in the ARIA DPM. Method 2) is similar, but samples the value within a polygon boundary, such as the Microsoft DPM. In the case of 3), the nearest point was chosen, where points outside a 10-m buffer were excluded to prevent misidentification. For 4), the centroid is chosen to represent the whole polygon to avoid edge effects from the raster being sampled. Some datasets, such as SAOCOM and EEFIT, did not overlap in geographic coverage and could not be compared.

C. Aligning Geographic Locations of Datasets Using Field Photographs to Integrate for Cross-Analysis

We also examined locations where multiple datasets overlap. Specifically, we tied these datasets to the Microsoft dataset, which includes both building footprints and damage values, to ensure that the same location was being measured. First, the locations of the data points derived from the EEFIT survey were manually verified, and associated with the building footprints, which comprised several steps. The appearance of each building was identified using photographs taken in the field and Google Street View, and their geographic location was determined using MAXAR, Google, and Bing optical satellite imagery. The most useful features for identification included roofs, windows, building shape, and orientation, as well as nearby objects, such as trees, signs, or flagpoles. We updated the metadata of the Microsoft footprint that had the best fit to the optical view of the building to include the damage grade from the EEFIT survey. In
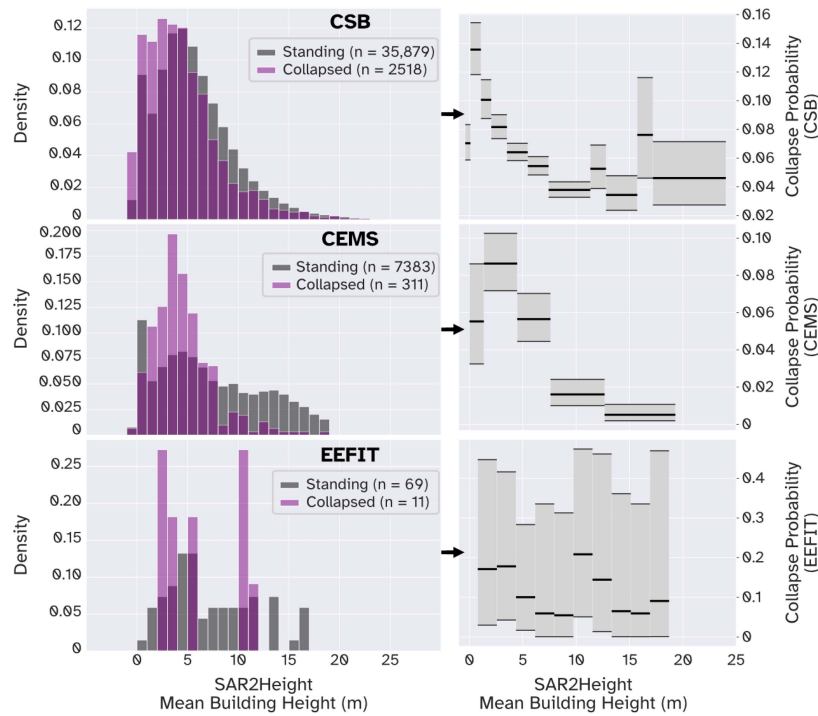
Fig. 5.   Building collapse probability distributions for heights obtained from the SAR2Height [17] algorithm. Left: density histograms of mean heights within OpenStreetMap building footprints, where standing (grey) and collapsed (purple) classes are displayed separately. Areas of overlap appear dark purple. The damage grades considered as "standing" or "collapsed" for the CSB, CEMS, and EEFIT datasets are given in Table II. The number of buildings (*n*) included in each class is provided. Right: Bayesian histograms generated from each pair of standing and collapsed distributions. The dark black lines represent the estimated collapse probability for each bin. 98% confidence intervals are visualized as vertical grey bars for each bin.
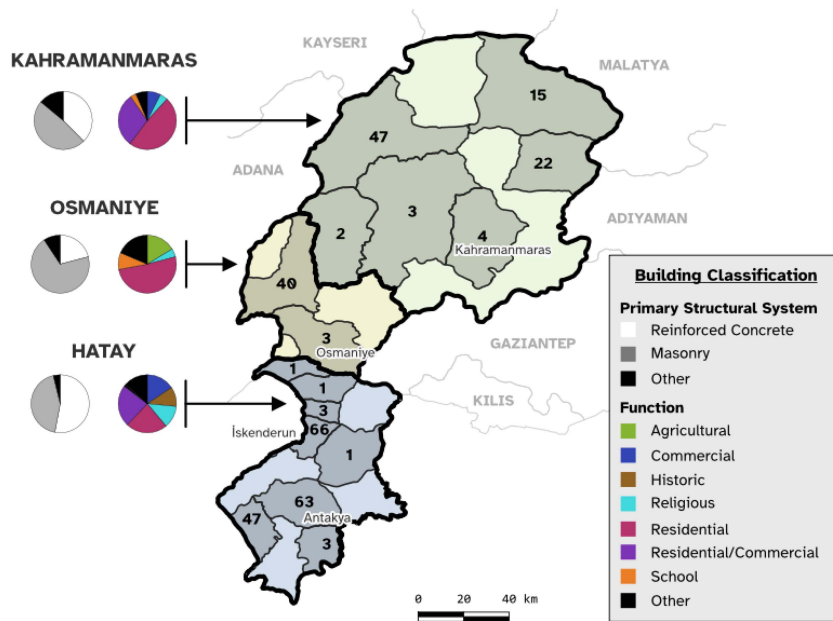

Fig. 6.   Locations of buildings surveyed by EEFIT from 13–17 March covering three provinces in Türkiye. The total number of surveyed buildings within each Level 2 administrative boundary is indicated. The primary structural systems and function of the buildings for each province are visualized with pie charts.

total, 206 buildings were able to be manually identified. After associating the EEFIT and Microsoft damage assessments in this fashion, we found that, of all datasets we deployed for the purpose of this article, only the CSB and ARIA DPM significantly overlapped these same buildings. We identified all CSB points that intersected the building footprints and took the

mean of the ARIA raster within each building footprint. The result is a collection of photographically verified buildings that intersect as many of the DPMs as possible. Given the different scales and units of measurement of these four datasets (e.g., ordinal for CSB but ratio for Microsoft), we normalized all the measurements to be between 0 and 1. Finally, for every building,
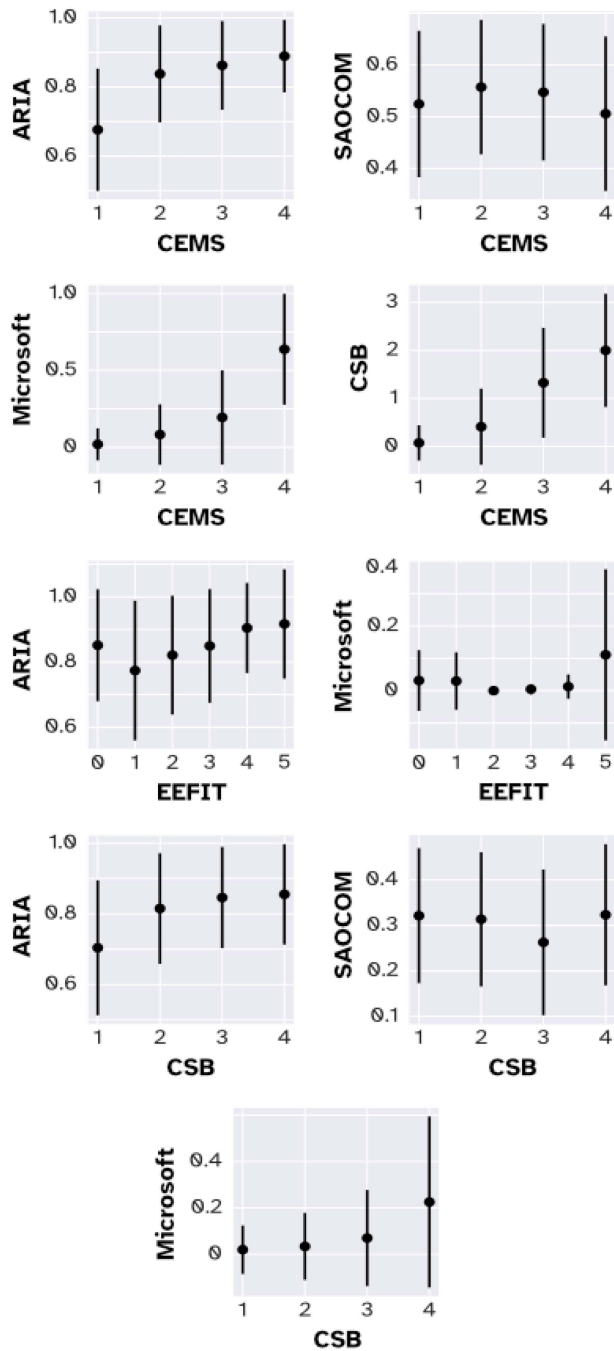
Fig. 7. Cross-comparison of damage maps. Damage grades for the CEMS, EEFIT, and CSB datasets are plotted on each x-axis. For each category on the x-axis, the corresponding mean values for each of the damage maps are plotted on the y-axis, with error bars representing ±1 standard deviation within each damage grade.

Fig. 8. Pairwise Euclidean distances between normalized building damage values for datasets that coincide within the same location.

we found the Euclidean distance between the normalized scores for all datasets, using the scikit-learn library in Python [35].

D. Collapsed Building Detection Using Machine Learning

We use machine-learning RF models [14] to explore the binary classification of buildings into two classes: one representing a standing building and another representing a "collapsed" or
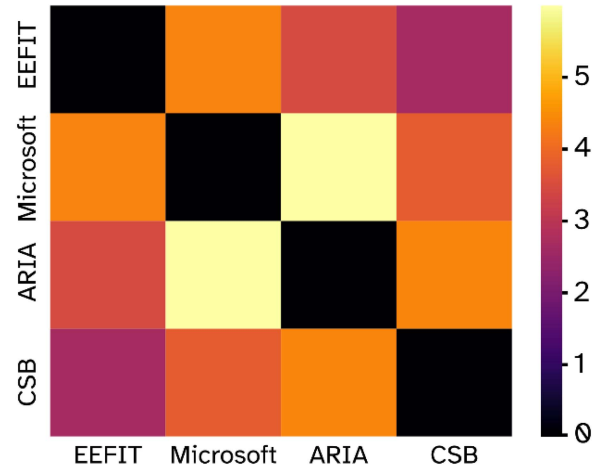
"destroyed" building. The CEMS, CSB, and EEFIT datasets had their damage grades redefined into "standing" and "collapsed" classes, where only the highest damage grade represented collapse, and all other grades represented a standing building (Table II). In CEMS, the highest damage grade represents a "destroyed" building, for CSB the highest grade represents a "collapsed" building, and in the EEFIT survey the highest grade represents "destruction." We compared locations where the random RF intersect the reclassified datasets, as well as where the reclassified datasets intersect each other.

Furthermore, we investigated the ability of building height maps obtained using CNNs from the SAR2Height algorithm [17] to detect building collapse. Height maps derived from 29 Umbra Space VHR SAR images were cropped to building footprints from OpenStreetMap [21]. We calculated the mean height within each footprint and determined the binary class of damage grades (Table II) that were found within each footprint. Afterword, each building footprint can be described by the average height value as well as the collapsed/standing classification from each of the CEMS, CSB, and EEFIT datasets (Fig. 5, left). We used the distribution of collapsed buildings and the distribution of standing buildings to create a probability distribution using Bayesian inference. Using Bayesian histograms, the probability of a rare event can be estimated [36]. We applied the method in [36] to our histograms of standing and collapsed buildings, to produce a distribution of building collapse probability for a given height output from the SAR2Height algorithm (Fig. 5, right). For the Bayesian histogram, an arbitrary, large number of bins (i.e., 50) are created, then are iteratively pruned to remove statistically insignificant bins. After that, the SAR2Height image can be converted to a probability map by mapping the height of each pixel into a probability based on the Bayesian histograms.

IV. RESULTS

The final recommendation for the field survey mission comprised six high-priority and five low-priority AOIs. Cities with a higher variance within each DPM, and with a large difference
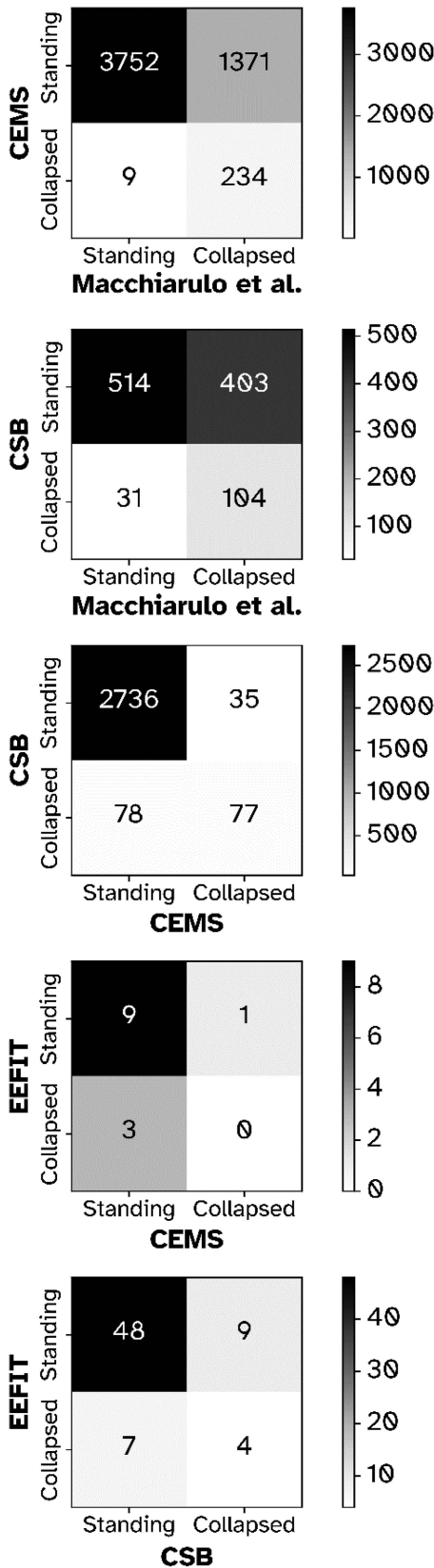
Fig. 9. Comparison of binary classification (collapsed or standing). The CEMS, CSB, and EEFIT data were converted into binary classes (Table II) and compared to the Macchiarulo et al. [14] RF building classes, as well as between each other, where possible.
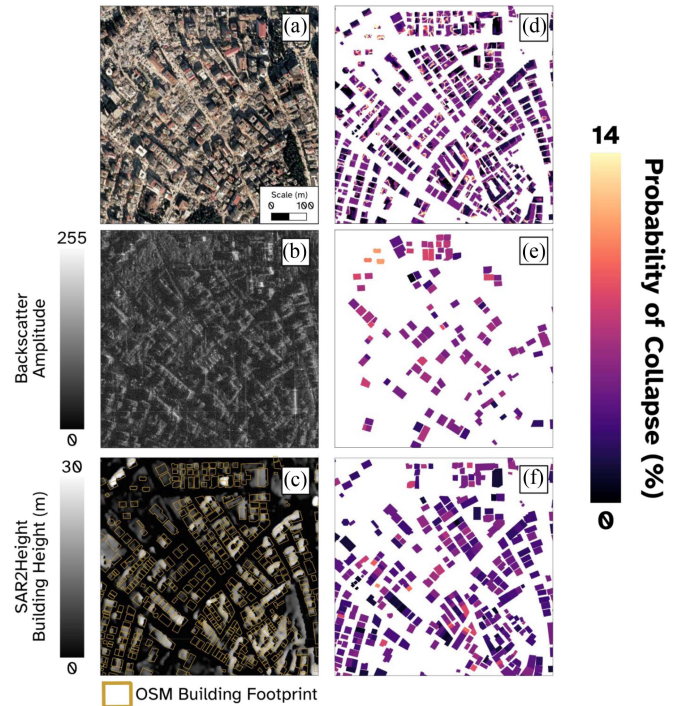

Fig. 10. Probability map results using the Bayesian histogram method. The scene is located in Antakya at 36° 12′ 24.24″N, 36° 09′ 22.33″E. (a) 30-cm resolution MAXAR optical image acquired on 11 February 2023. (b) Umbra SAR image acquired over the same area on 05 March 2023, at 30-cm resolution. (c) SAR2Height [17] results for the Umbra SAR image. (d) Collapse probability distribution, derived from Bayesian histogram for the CSB data (Fig. 5), was mapped to the SAR2Height building heights and clipped to the OpenStreetMap building footprints. (e) Mean probability for destroyed buildings. (f) Mean probability for buildings that are not destroyed.

Fig. 11. Building with a damage grade of 4 on the EMS-98 scale in Antakya with damaged sides. Panel A is a photograph from the 13–17 March 2024 survey. Panel B is a MAXAR image on 8 February 2024 of the same building, with building footprints from the Microsoft dataset [26]. The footprint of the building is displayed in red. Despite being classified as "very heavy damage" in the field survey, the AI-based damage assessment computed the damage as 0%.

between DPMs, were prioritized (Fig. 4). The high-priority AOIs were located near the cities of Islahiye, Kahramanmaraş, Nurdağı, Bahçe, Osmaniye, and İskenderun. Additionally, Antakya was prioritized due to the close agreement of damage variances across DPMs, which remained moderately elevated. The low-priority AOIs of Adıyaman, Kilis, Malatya, Şanlıurfa, and Gaziantep had a lower diversity of damage and building characteristics but were proposed due to their proximity to the high-priority targets for various EEFIT field subteams, including

geotechnics, structural response, and recovery characteristics, and therefore presented an opportunity to increase the data volume if time permitted [2]. Based on these recommendations, the field team of 15 members was deployed to the target areas on 13–17 March to perform detailed damage assessments (Fig. 6). Due to logistical constraints (travel difficulties across a large area exacerbated by infrastructure failures) and limited time available for the field surveys, it was not possible to visit every region. Regardless, 330 structures were surveyed by the field team as a representative sample of heights, ages, damage grades, and material.

In the paired analysis (Fig. 7), the various damage maps were compared with categorical damage grades. As the CEMS data were created by human labelers, and the CSB and EEFIT damage grades derive from ground surveys, they may serve as validation data. In each plot, the mean damage value for the *y*-axis data is plotted for each category on the *x*-axis, with standard deviation bars. The damage grades are given as integers, with larger integers representing higher degrees of damage. Good agreement between the DPMs would be indicated with a linear trend, where higher damage values in one dataset correspond to higher values in the other. The best agreement was between CSB and CEMS and between Microsoft and CEMS, with correlation coefficients of 0.65 and 0.62, respectively. The correlation between ARIA and CEMS was 0.31, correlation between Microsoft and CSB was 0.29, and correlation between ARIA and CSB was 0.28. In all other cases, the correlation coefficient between the datasets is under 0.2.

For the 206 building locations verified by field photographs (Section III-C), the Euclidean distance between normalized scores was computed between all datasets. The distances are presented in matrix form in Fig. 8. Each cell represents the distance between the damage values of two datasets. Lower distances indicated greater agreement. The ground-based assessments have the lowest distance, while the greatest distance is between the Microsoft and ARIA data.

Fig. 9 displays confusion matrices for the binary damage maps created by the RF approach as well as with the CEMS, CSB, and EEFIT damage records, wherever any two datasets had significant geographic overlap. The RF method [14] had an overall accuracy of 74.3% when compared to CEMS, and 58.7% when compared to CSB. An accuracy of 96.1% was achieved between the CSB and CEMS datasets. The EEFIT data did not coincide with many CEMS points but had 76.5% accuracy compared to CSB.

In Fig. 5, density histograms of AI-derived SAR2Height [17] building heights are plotted for buildings that are standing, and those that are collapsed. The labels for the collapsed and standing buildings are derived from the CSB, CEMS, and EEFIT datasets. A Bayesian approach (Section III-D) is used calculate probability of collapse for a given building height. This probability distribution can be mapped to the SAR2Height image within the building footprints. Fig. 10, Panel A, shows a MAXAR image of an area in downtown Antakya where this method was applied. Panel B displays the Umbra image that is the input to the SAR2Height algorithm, while Panel C displays

the resulting height map. Then, each height pixel is mapped to a probability using the Bayesian histogram for the CSB data (Fig. 5, right) and clipped to the boundaries of the building footprints from OpenStreetMap (Fig. 10, Panel D). Out of the three histograms, CSB achieved the highest probability estimate and thus was chosen to create the probability map. Fig. 10, Panels E and F display the mean probability for buildings that are labeled as destroyed and as not destroyed, respectively. The destroyed building polygons are sourced from the HOT [37].

V. Conclusion

Our approach uses predefined geographic units, such as administrative boundaries (Fig. 1), as a frame of reference to apply summary statistics to a wide region, employing datasets with widely variable resolutions and data formats (Table I, Figs. 2–3). While such boundaries can provide a broad outline of the region (Fig. 3), a city-by-city analysis in terms of variance of damage is required for choosing the top AOI for ground-based survey teams in a postdisaster reconnaissance study (Fig. 4). While our current maps can effectively translate satellite remote sensing data into actionable city-scale recommendations (Figs. 4 and 6), they do not take into consideration logistics in the field. Road closures or infrastructure failures due to the impact of an earthquake and/or as a result of cascading hazards postearthquake, as in the February 2023 Türkiye Earthquakes, are a particular concern, which could influence the choice of an AOI if a given city is not reachable by the ground-based team [2].

Interoperability between disparate data formats remains a challenge for providing rapid and comprehensive postdisaster assessment, regarding the damage to the built environment. While we make a comparison of the values of damage maps for the February 2023 earthquakes (Figs. 7–9), the variation of characteristics between the damage maps in this article should be emphasized. The units of measurement represent different quantities (i.e., percent of roof damage vs. difference in interferometric coherence) and are produced from sources with differing radiometric and physical image formation principles (i.e., SAR vs. electro-optical). The pixel spacing of DPM images considered here ranged from the order of 30 m to under 1 m. Vector data in point and polygon format may not directly overlap, causing ambiguity in building locations and relative geocoding errors. Additionally, ground-based surveys that use GNSS receivers to record building locations can be affected by multipath and nonline-of-sight errors [38], [39], potentially leading to misidentification of buildings when compared to building inventories.

Furthermore, remote sensing methods struggle to achieve meaningful intermediary classifications of damage between standing and collapsed (Fig. 7). Because optical satellites look in the nadir direction, often only building rooftops are visible. This can result in misclassification of the damage level if there is significant structural damage at the sides of the building that are not visible from above (Fig. 11). SAR has a side-looking geometry and may be able to overcome this limitation, but how to best leverage this attribute is currently underexplored. In

addition, resolution at submeter (VHR) is required to acquire information on building sides, often coming from commercial satellites, meaning data availability is a major limiting factor.

The SAR-based DPMs created from Sentinel-1 (ARIA) and SAOCOM had pixel spacing (30 and 7 m, respectively) that rendered them unable to characterize damage at the building scale (Fig. 7). When compared to the EEFIT data, the ARIA DPM was not sensitive to changes in damage grades. The lowest values of the ARIA DPM corresponded to the lowest CEMS class (no visible damage) and CSB class (slightly damaged), although in both cases the difference is within the range of standard deviation. The SAOCOM DPM does not show a trend in relation to the observed damage grades with the CEMS or CSB data. This could be due to the high temporal baseline between the coseismic SAOCOM images, or the different temporal baseline between preseismic and coseismic images, highlighting the importance of routine global acquisitions when considering InSAR DPM products. Additionally, even though the analysis was restricted to urban areas using the Global Urban Footprint [40] to city boundaries, urban vegetation may still cause temporal decorrelation, and local topography can influence the value of the DPM [15]. This suggests that SAR data at these resolutions are best for detecting larger regions of collapsed or destroyed infrastructure, although it is important to consider the limitations of the satellite repeat period and temporal decorrelation.

The best correlation between datasets was between the Microsoft AI-based method and CEMS, both of which used optical VHR data (Fig. 7). The CEMS data showed a similar level of agreement with CSB. Even so, intermediate damage classes are still within the range of the standard deviation bars, meaning the trend is uncertain. Using the data that were manually verified to co-occur at the same building using the field photographs (Section III-C), the ground-based EEFIT and CSB damage grades had the closest Euclidean distance between each other, at 2.6 (Fig. 8), despite the underrepresentation of moderate damage cases in the CSB dataset. Of all datasets we use in this article, these are the only two obtained as a result of in-person/field damage assessment, which may be argued to contribute to this close agreement. This increases to a maximum of 6.0 between Microsoft and ARIA, showing how damage maps that use different data sources and analysis techniques can provide drastically different assessments. All these results also underscore the difficulty of reliably classifying intermediate damage levels within different ground-based validation datasets and with current remote sensing techniques, even with VHR data. Additionally, there is variability among operators in how they define intermediate classes (Table II).

Binary classification has typically been considered more suitable for remote sensing data [24], [41], because these data are limited to an overhead view and often lack sufficient resolution. Additionally, identification of collapsed structures is the most urgent priority in rapid response scenarios. Therefore, we compared collapsed and standing classes between the RF method, and the existing CEMS, CSB, and EEFIT damage assessments (Fig. 9). The highest damage grade of the latter three datasets was given the "collapsed" class, while the remaining classes were assigned "standing" (Table II). Of particular concern are false negatives, since incorrectly classifying a collapsed building as standing could delay emergency response and cost lives. The RF approach [14] had a false negative rate (FNR) of just 3.7% when compared to CEMS, and 23.0% when compared to CSB. When compared to the CSB data, CEMS had an FNR of 50.3%. It is promising to observe a low FNR with an automated approach (RF) when compared to the labels from CEMS. However, this is qualified by the fact that CEMS is derived from satellite data, and the actual FNR of CEMS when compared to ground-based CSB was higher, at 50.3%, even if the overall accuracy of CEMS was high at 96.1%. In addition, although the underrepresentation of moderate damage cases in the CSB data is a concern, this is mitigated by only taking the highest damage grade as the "collapsed" class. Overall, this highlights the possibility of the published CSB map being preliminary (See Section II-F) or the subjectivity inherent in damage assessment, even ground-based, as manually generated labels can vary. Another issue is that the definition of a "collapsed" and "destroyed" building can be different between methodologies and may be subjectively interpreted differently, depending on the size or height of a building.

The SAR2Height map was proposed here for the first time in an operational scenario for classifying collapsed buildings where no LIDAR DEMs are available. The underlying idea is that, with a minimal validation dataset distinguishing between collapsed vs. standing buildings it is possible to characterize the probability of collapse of a building using an existing Bayesian framework, which has originally been used with SAR for flood modeling [42], [43], [44], [45]. The EEFIT data were too sparse to provide a probability map (Fig. 5). The CEMS data could not provide a collapse probability higher than 12.7%, while the CSB could not provide a probability higher than 13.7%. The CSB data were able to achieve a larger number of significantly different Bayesian histogram bins, likely due to the higher number of data points. Since intermediate damage classes are not considered for this probability map, the impact of the CSB data being biased toward low damage and heavy damage classes may be attenuated. As yet, the Bayesian probability maps generated from the SAR2Height building heights (Fig. 10) are not sufficient for real-world scenarios. The maximum collapse probability being under 14% represents a low-degree confidence in the model predictions. Many destroyed buildings [Fig. 10(e)] were characterized by low probabilities, while many nondestroyed buildings had elevated probabilities, according to the model. These results suggest that, as with all the discussed methodologies, high-quality validation data are necessary as building height is not the only discriminant for identifying collapsed buildings. Precise coregistration of the height map to building footprints will be required to increase the accuracy of these predictions, which is a particular issue for SAR data. Because SAR is side-looking, building locations are often displaced when compared to building footprint data [13], [46]. Therefore, inaccurate alignment between the SAR data and footprints will result in the conflation of ground pixels with building pixels.

Furthermore, while multisensor approaches based on radar and optical observations could improve multiclass detection [47], they inherently increase dataset codependency which might increase the data latency of the final damage products. Smallsat constellations, with the ability to direct the sensor to a particular AOI, present a unique opportunity for rapid response scenarios. Traditional satellite systems can only image an area after a certain repeat interval (6 or 12 days for Sentinel-1, and 8 days for SAOCOM), meaning a postearthquake acquisition may take several days. In addition to providing VHR data, Smallsat missions can overcome this issue.

In conclusion, future earthquake response missions could benefit from a harmonized approach between damage assessment products. It will be necessary to further elucidate the relationship between values obtained from the varied methodologies for producing damage maps, allowing greater opportunities for data fusion. Errors in data-position should be minimized, and accurate building footprint data are necessary. Footprints may need to be accurately coregistered, especially for SAR data. Locations and timing of damage maps and validation data should be as concurrent as possible to strengthen quality assurance procedures.

Acknowledgment

References

[1] Y. Aktas et al., "Hybrid EEFIT mission to February 2023 Kahramanmaraş earthquake sequence," in *Proc. SECED Conf. Earthq. Eng. Dyn. Sustain. Future*, Sep. 2023, pp. 1–10.

[2] Y. D. Aktas et al., "The Türkiye earthquake sequence of February 2023: A longitudinal study report by EEFIT," EEFIT, Feb. 2024. [Online]. Available: https://www.istructe.org/resources/report/eefit-mission-report-Turkey-february-2023/

[3] Y. D. Aktas et al., "Hybrid reconnaissance mission to the 30 October 2020 Aegean sea earthquake and Tsunami (Izmir, Turkey & Samos, Greece): Description of data collection methods and damage," *Front. Built Environ.*, vol. 8, Jul. 2022, Art. no. 840192, doi: 10.3389/fbuil.2022.840192.

[4] M. R. Z. Whitworth et al., "Lessons for remote post-earthquake reconnaissance from the 14 August 2021 Haiti earthquake," *Front. Built Environ.*, vol. 8, Apr. 2022, Art. no. 873212, doi: 10.3389/fbuil.2022.873212.

[5] Y. D. Aktas and E. So, "Editorial: Disaster reconnaissance missions: Is a hybrid approach the way forward?," *Front. Built Environ.*, vol. 8, Jul. 2022, Art. no. 954571, doi: 10.3389/fbuil.2022.954571.

[6] E. M. Rathje and K. Franke, "Remote sensing for geotechnical earthquake reconnaissance," *Soil Dyn. Earthq. Eng.*, vol. 91, pp. 304–316, Dec. 2016, doi: 10.1016/j.soildyn.2016.09.016.

[7] S. Wilkinson et al., "How can new technologies help us with earthquake reconnaissance?," in *Proc. 11th Nat. Conf. Earthq. Eng.*, Jan. 2018, pp. 3027–3035.

[8] J. D. Bray, J. D. Frost, E. M. Rathje, and F. E. Garcia, "Recent advances in geotechnical post-earthquake reconnaissance," *Front. Built Environ.*, vol. 5, Jan. 2019, Art. no. 5, doi: 10.3389/fbuil.2019.00005.

[9] D. Contreras, S. Wilkinson, and P. James, "Earthquake reconnaissance data sources, a literature review," *Earth*, vol. 2, no. 4, pp. 1006–1037, Nov. 2021, doi: 10.3390/earth2040060.

[10] D. Contreras, S. Wilkinson, Y. D. Aktas, L. Fallou, R. Bossu, and M. Landès, "Intensity-based sentiment and topic analysis. The case of the 2020 Aegean earthquake," *Front. Built Environ.*, vol. 8, Mar. 2022, Art. no. 839770, doi: 10.3389/fbuil.2022.839770.

[11] R. Spence, "The full-scale laboratory: The practice of post-earthquake reconnaissance missions and their contribution to earthquake engineering: The third Nicholas Ambraseys lecture," in *Perspectives on European Earthquake Engineering and Seismology* (Geotechnical, Geological and Earthquake Engineering), vol. 34, A. Ansal, Ed. Berlin, Germany: Springer, 2014, pp. 1–52, doi: 10.1007/978-3-319-07118-3_1.

[12] G. Giardina et al., "Combining remote sensing techniques and field surveys for post-earthquake reconnaissance missions," *Bull. Earthq. Eng.*, vol. 22, pp. 3415–3439, 2024, doi: 10.1007/s10518-023-01716-9.

[13] Y. Sun, Y. Wang, and M. Eineder, "QuickQuakeBuildings: Post-earthquake SAR-optical dataset for quick damaged-building detection," 2023, *IEEE Geosci. Remote Sensing Lett.*, vol. 21, pp. 1–5, 2024, doi: 10.1109/LGRS.2024.340696.

[14] V. Macchiarulo, G. Giardina, P. Milillo, Y. D. Aktas, and M. R. Z. Whitworth, "Integrating post-event very high resolution SAR imagery and machine learning for building-level earthquake damage assessment," *Bull. Earthq. Eng.*, to be published, doi: 10.1007/s10518-024-01877-1.

[15] S.-H. Yun et al., "Rapid damage mapping for the 2015 M_w 7.8 Gorkha earthquake using synthetic aperture radar data from COSMO–SkyMed and ALOS-2 satellites," *Seismological Res. Lett.*, vol. 86, no. 6, pp. 1549–1556, Nov. 2015, doi: 10.1785/0220150152.

[16] P. Milillo, B. Riel, B. Minchew, S.-H. Yun, M. Simons, and P. Lundgren, "On the synergistic use of SAR constellations' data exploitation for earth science and natural hazard response," *IEEE J. Sel. Topics Appl. Earth Observ. Remote Sens.*, vol. 9, no. 3, pp. 1095–1100, Mar. 2016, doi: 10.1109/JSTARS.2015.2465166.

[17] M. Recla and M. Schmitt, "The SAR2Height framework for urban height map reconstruction from single SAR intensity images," *ISPRS J. Photogrammetry Remote Sens.*, vol. 211, pp. 104–120, May 2024, doi: 10.1016/j.isprsjprs.2024.03.023.

[18] *Türkiye - Subnational Administrative Boundaries*. United Nations Office for the Coordination of Humanitarian Affairs, Humanitarian Data Exchange, 2023. [Online]. Available: https://data.humdata.org/dataset/cod-ab-tur

[19] T. Esch et al., "World settlement footprint 3D—A first three-dimensional survey of the global building stock," *Remote Sens. Environ.*, vol. 270, Mar. 2022, Art. no. 112877, doi: 10.1016/j.rse.2021.112877.

[20] M. Marconcini, A. Metz-Marconcini, T. Esch, and N. Gorelick, "Understanding current trends in global urbanisation—The world settlement footprint suite," *Giforum*, vol. 1, pp. 33–38, 2021, doi: 10.1553/giscience2021_01_s33.

[21] *Turkey Buildings (OpenStreetMap Export)*. United Nations Office for the Coordination of Humanitarian Affairs, 2023. [Online]. Available: https://data.humdata.org/dataset/hotosm_tur_buildings?

[22] *EMSR648: Earthquake in East Anatolian Fault Zone*. Copernicus Emergency Management Service, 2023. [Online]. Available: https://emergency.copernicus.eu/mapping/list-of-components/EMSR648

[23] G. Grünthal, *European Macroseismic Scale 1998*. European Seismological Commission (ESC), 1998.

[24] S. Cotrufo, C. Sandu, F. Giulio Tonolo, and P. Boccardo, "Building damage assessment scale tailored to remote sensing vertical imagery," *Eur. J. Remote Sens.*, vol. 51, no. 1, pp. 991–1005, Jan. 2018, doi: 10.1080/22797254.2018.1527662.

[25] I. Joubert-Boitat, A. Dalmasso, and S. Wania, "Manual for CEMS-rapid mapping products," *Publications Office of the European Union*, no. EUR 30370 EN, Sep. 2020, [Online]. Available: https://data.europa.eu/doi/10.2760/29876

[26] C. Robinson et al., "Turkey earthquake report," Microsoft, MSR-TR-2023-7, Feb. 2023. [Online]. Available: https://www.microsoft.com/en-us/research/publication/Turkey-earthquake-report/

[27] H. A. Zebker and J. Villasenor, "Decorrelation in interferometric radar echoes," *IEEE Trans. Geosci. Remote Sens.*, vol. 30, no. 5, pp. 950–959, Sep. 1992, doi: 10.1109/36.175330.

[28] R. F. Hanssen, *Radar Interferometry: Data Interpretation and Error Analysis* (Remote Sensing and Digital Image Processing), vol. 2. Berlin, Germany: Springer, 2001, doi: 10.1007/0-306-47633-9.

[29] *ARIA Share*. NASA Jet Propulsion Laboratory, 2023. [Online]. Available: https://aria-share.jpl.nasa.gov/20230206_Turkey_EQ/DPM/

[30] *Exitoso Lanzamiento del Satélite SAOCOM 1A*. CONAE, 2018. [Online]. Available: https://www.Argentina.gob.ar/noticias/exitoso-lanzamiento-del-satelite-saocom-1a

[31] R. M. Haralick, K. Shanmugam, and I. Dinstein, "Textural features for image classification," *IEEE Trans. Syst., Man, Cybern.*, vol. SMC-3, no. 6, pp. 610–621, Nov. 1973, doi: 10.1109/TSMC.1973.4309314.

[32] "GlobalMLBuildingFootprints," Microsoft, 2023.

[33] *2023 Turkey Earthquakes Building Damage Assessment Map*. 2023. [Online]. Available: https://studio.foursquare.com/public/9fdbbd16-cd10-46dc-b099-d43d75f74a9d

[34] K. He, X. Zhang, S. Ren, and J. Sun, "Deep residual learning for image recognition," in *Proc. 2016 IEEE Conf. Comput. Vis. Pattern Recognit. (CVPR)*, Las Vegas, NV, USA, 2016, pp. 770–778, doi: 10.1109/CVPR.2016.90.

[35] F. Pedregosa et al., "Scikit-learn: Machine learning in Python," *J. Mach. Learn. Res.*, vol. 12, pp. 2825–2830, Nov. 2011.

[36] D. Häfner, J. Gemmrich, and M. Jochum, "Real-world rogue wave probabilities," *Sci. Rep.*, vol. 11, no. 1, May 2021, Art. no. 10084, doi: 10.1038/s41598-021-89359-1.

[37] *HOTOSM Turkey Destroyed Buildings (OpenStreetMap Export)*, United Nations Office for the Coordination of Humanitarian Affairs, Humanitarian Data Exchange, 2023. [Online]. Available: https://data.humdata.org/dataset/hotosm_tur_destroyed_buildings?

[38] P. Xie and M. G. Petovello, "Measuring GNSS multipath distributions in urban canyon environments," *IEEE Trans. Instrum. Meas.*, vol. 64, no. 2, pp. 366–377, Feb. 2015, doi: 10.1109/TIM.2014.2342452.

[39] D. Weng, Z. Hou, Y. Meng, M. Cai, and Y. Chan, "Characterization and mitigation of urban GNSS multipath effects on smartphones," *Measurement*, vol. 223, Dec. 2023, Art. no. 113766, doi: 10.1016/j.measurement.2023.113766.

[40] T. Esch et al., "Breaking new ground in mapping human settlements from space—The global urban footprint," *ISPRS J. Photogrammetry Remote Sens.*, vol. 134, pp. 30–42, Dec. 2017, doi: 10.1016/j.isprsjprs.2017.10.012.

[41] A. Huynh, M. Eguchi, A. Y.-M. Lin, and R. Eguchi, "Limitations of crowdsourcing using the EMS-98 scale in remote disaster sensing," in *Proc. IEEE Aerosp. Conf.*, Mar. 2014, pp. 1–7, doi: 10.1109/AERO.2014.6836457.

[42] L. Giustarini et al., "Probabilistic flood mapping using synthetic aperture radar data," *IEEE Trans. Geosci. Remote Sens.*, vol. 54, no. 12, pp. 6958–6969, Dec. 2016, doi: 10.1109/TGRS.2016.2592951.

[43] Y. N. Lin, S.-H. Yun, A. Bhardwaj, and E. M. Hill, "Urban flood detection with Sentinel-1 multi-temporal synthetic aperture radar (SAR) observations in a Bayesian framework: A case study for hurricane Matthew," *Remote Sens.*, vol. 11, no. 15, Jul. 2019, Art. no. 1778, doi: 10.3390/rs11151778.

[44] S. F. Sherpa, M. Shirzaei, C. Ojha, S. Werth, and R. Hostache, "Probabilistic mapping of August 2018 flood of Kerala, India, using spaceborne synthetic aperture radar," *IEEE J. Sel. Topics Appl. Earth Observ. Remote Sens.*, vol. 13, pp. 896–913, Feb. 2020, doi: 10.1109/JSTARS.2020.2970337.

[45] S. F. Sherpa and M. Shirzaei, "Country-wide flood exposure analysis using sentinel-1 synthetic aperture radar data: Case study of 2019 Iran flood," *J. Flood Risk Manage.*, vol. 15, no. 1, Mar. 2022, Art. no. e12770, doi: 10.1111/jfr3.12770.

[46] Y. Sun, S. Montazeri, Y. Wang, and X. X. Zhu, "Automatic registration of a single SAR image and GIS building footprints in a large-scale urban area," *ISPRS J. Photogrammetry Remote Sens.*, vol. 170, pp. 1–14, Dec. 2020, doi: 10.1016/j.isprsjprs.2020.09.016.

[47] X. Yu et al., "Intelligent assessment of building damage of 2023 Turkey–Syria earthquake by multiple remote sensing approaches," *NPJ Natural Hazards*, vol. 1, no. 1, Mar. 2024, Art. no. 3, doi: 10.1038/s44304-024-00003-0.

Pietro Milillo (Senior Member, IEEE) received the bachelor's (Laurea) and master's degrees in physics, with a thesis on synthetic aperture radar and GPS data processing, from the University of Bari, Bari, Italy, in 2010 and 2012, respectively, and the Ph.D. degree in environmental engineering, with a thesis on the synergistic use of synthetic aperture radar constellations for studying natural and anthropogenic phenomena, from the University of Basilicata, Potenza, Italy, in 2016.

Over the years, he has held various positions, including a NASA Postdoctoral Program Fellow with the Jet Propulsion Laboratory (JPL), California Institute of Technology, a Scientist in radar science and engineering with the JPL, and an Associate Project Scientist in Earth system science with the University of California, Irvine, CA, USA. Since 2021, he has been an Assistant Professor in Civil and Environmental Engineering with the Department of Civil and Environmental Engineering, University of Houston (UH), Houston, TX, USA. He is also a Guest Scientist with the German Aerospace Center (DLR), Munich, Germany, and an Adjunct Professor in Earth and Atmospheric Science with the UH. He has authored or coauthored more than 50 research articles in leading international journals. His research interests include synergistic use of remote sensing data exploitation and innovative approaches for computational analyses in Earth and cryosphere science and natural/anthropogenic hazard response. He is particularly interested in analyzing how the new generation of remote sensing instruments leads to a more effective, near real-time disaster monitoring, assessment, and response. His research interests [funded by NASA, DLR, and the Italian Space Agency (ASI)] also include Earth science, cryosphere, and disaster response.

Amin Tavakkoliestahbanati received the B.S. degree in geodesy and geomatics engineering from the Esfahan University, Isfahan, Iran, in 2014, and the M.Sc. degree in remote sensing from the Shiraz University, Shiraz, Iran, in 2016. He is currently working toward the Ph.D. degree in geosensing systems engineering & sciences with the University of Houston, Houston, TX, USA.

His research interests include SAR interferometry applications in deformation monitoring.

Brandon Voelker received the B.S. degree (magna cum laude) in environmental science with a geoscience focus from the University of Washington, Seattle, WA, USA, in 2019, and the M.S. degree in geosensing systems engineering & sciences from the University of Houston, Houston, TX, USA, in 2023.

He is currently working as a full-time Research Assistant with the University of Houston.

Valentina Macchiarulo (Member, IEEE) received the B.Sc. and M.Sc. degrees in aerospace engineering from the University of Rome La Sapienza, Rome, Italy, in 2013 and 2016, respectively, and the Ph.D. degree in civil engineering, with a thesis focused on integrating satellite radar interferometry with civil engineering procedures to assess building and infrastructure conditions on a regional scale, from the University of Bath, Bath, U.K., in 2022.

Between 2016 and 2017, she was a Student Fellow with the National Autonomous University of Mexico (UNAM), Mexico City, Mexico, and the National Laboratories of Frascati (INFN-LNF), Frascati, Italy. In 2019, during her doctoral training, she was a Visiting Researcher with NASA's Jet Propulsion Laboratory (JPL), Pasadena, CA, USA. She is currently a Research Associate with the Delft University of Technology, Delft, The Netherlands. Her research interests include remote sensing, geospatial analysis, computational modeling, and machine learning, with a focus on urban and infrastructure resilience and hazard-impact mitigation.

Giorgia Giardina received the M.S. degree (summa cum laude) in environmental engineering from the University of Brescia, Brescia, Italy, in 2007, and the Ph.D. degree in civil engineering from the Delft University of Technology, Delft, The Netherlands, in 2013.

She is currently an Associate Professor in Geo-Monitoring and Data Analytics with the Delft University of Technology and the "Sensing from Space" Theme Leader of the Delft Space Institute, Delft, The Netherlands. Previously, she was an Assistant Professor with the University of Bath, Bath, U.K., a Visiting Professor with the NASA Jet Propulsion Laboratory, La Cañada Flintridge, CA, USA, and a Research Associate with the University of Cambridge, Cambridge, U.K. Her research interests include remote sensing and computational modeling, multihazard risk and damage assessment, heritage protection, and infrastructure resilience.

Dr. Giardina is a member of the Earthquake Engineering Field Investigation Team management committee, the International Scientific Committee on the Analysis and Restoration of Structures of Architectural Heritage, the Centre for Global Heritage and Development, and the 4TU Centre for Resilience Engineering.

Michael Recla received the B.Sc. degree in geodesy and geoinformation from the Technical University of Munich (TUM), Munich, Germany, in 2018, and the M.Sc. degree in geodesy and geoinformation with a specialization in physical and satellite geodesy from the TUM, in 2021.

He is currently a full-time Research Assistant with the Earth Observation Lab, University of the Bundeswehr Munich, Neubiberg, Germany. His research interests include machine learning, computer vision, and radar remote sensing, and is partly funded by the German Research Foundation (DFG) and partly by Airbus Defence and Space.

Michael Schmitt received the Dipl.-Ing. (Univ.) degree in geodesy and geoinformation, the Dr.-Ing. degree in remote sensing, and the habilitation degree in data fusion from the Technical University of Munich (TUM), Munich, Germany, in 2009, 2014, and 2018, respectively.

Since 2021, he has been a Full Professor for Earth Observation with the Department of Aerospace Engineering, University of the Bundeswehr Munich (UniBw M), Neubiberg, Germany. From 2020 to 2022, he additionally held the position of a Consulting Senior Scientist with the Remote Sensing Technology Institute, German Aerospace Center (DLR), Cologne, Germany. Before joining the UniBw M, he was a Professor for Applied Geodesy and Remote Sensing with the Department of Geoinformatics, Munich University of Applied Sciences, Munich, Germany. From 2015 to 2020, he was a Senior Researcher and Deputy Head at the Professorship for Signal Processing in Earth Observation, TUM. In 2016, he was a Guest Scientist with the University of Massachusetts, Amherst, MA, USA. In 2019, he was additionally appointed as an Adjunct Teaching Professor with the Department of Aerospace and Geodesy, TUM. His research interests include technical aspects of Earth observation, in particular image analysis and machine learning applied to the extraction of information from multimodal remote sensing observations.

Prof. Schmitt is a co-chair of the Working Group "Active Microwave Sensing" of the International Society for Photogrammetry and Remote Sensing, and an active member of the Working Group "Benchmarking" of the IEEE-GRSS Image Analysis and Data Fusion Technical Committee. He frequently serves as a Reviewer for a number of renowned international journals and conferences and was the recipient of several Best Reviewer awards. He is a Senior Member of the IEEE and an Associate Editor of IEEE GEOSCIENCE AND REMOTE SENSING MAGAZINE as well as a Co-Editor of the *Springer Journal of Photogrammetry*, *Remote Sensing*, and *Geoinformation Science* (PFG). He is also a member of the Research Center SPACE and the Institute of Space Technology & Space Applications of UniBw M.

Marzia Cescon (Member, IEEE) received the B.Sc. degree in information engineering and the M.Sc. degree in control systems engineering from the University of Padua, Padua, Italy, in 2005 and 2008, respectively, and the Ph.D. degree in automatic control from the Automatic Control Department, Lund University, Lund, Sweden, in 2014.

She is the endowed David C. Zimmerman Assistant Professor of Mechanical and Aerospace Engineering with the University of Houston, Houston, TX, USA. She is the Founder and the Director of the Advanced Learning, Artificial Intelligence and Control laboratory, a multidisciplinary effort developing novel computational methods and tools for learning-based decision-making and control of complex and unknown dynamical systems. Her research interests include biomedical control systems, multiagent systems, and safe autonomy of cyberphysical systems. She has held several research positions with the University of California, Santa Barbara, CA, USA; the Melbourne School of Engineering, University of Melbourne, Melbourne, VIC, Australia; and the Harvard John A. Paulson School of Engineering and Applied Sciences, Harvard University, Cambridge, MA, USA.

Dr. Cescon was the recipient of the 2024 NSF CAREER award.

Yasemin D. Aktas received the B.Sc. degree in structural engineering from the Middle East Technical University (METU), Ankara, Türkiye, in 2003, the M.Sc. degree in heritage science from the METU, in 2006, and the Ph.D. degree in heritage conservation engineering from the METU, in 2011.

She is currently an Associate Professor in Applied Materials and Structures with the Department of Civil, Environmental and Geomatic Engineering, University College London, London, U.K. and the Deputy Academic Director of the U.K. Centre for Moisture in Buildings. Her research interests include disaster risk reduction, climate adaptation, and public health.

Dr Aktas is the Chair of the U.K.'s Earthquake Engineering Field Investigation Team, where she led/advised on several postdisaster reconnaissance studies, and is a Fellow of Royal Society for Public Health.

Emily So received the M.Eng. degree in civil engineering from the Imperial College London, London. U.K., in 1999, and the Ph.D. degree in architecture from the University of Cambridge, Cambridge, U.K., in 2009.

He is currently a Reader of architectural engineering with the University of Cambridge and the Director of the Cambridge University Centre for Risk in the Built Environment. She is a Chartered Civil Engineer with specialist experience in loss assessments earthquake engineering designs. She is an expert in the field of casualty estimation in earthquakes, and she is on the U.K. Scientific Advisory Group for Emergencies. Her research interests include estimating the dead and injured and proposes ways of improving data collection and modeling techniques.